THE JOURNAL OF PHYSICAL CHEMISTRY C
A JOURNAL OF THE AMERICAN CHEMICAL SOCIETY

pubs.acs.org/JPCC

Article

Temperature-Modulated Facet Orientation of Perovskite Films Using Controllable Moisture for Efficient Solar Cells

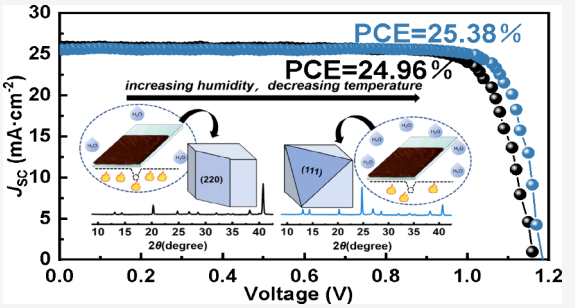
Hai-Fang Li, Zhiyu Zhang, Teng Xu, Shujie Qu, Chuanmin Yao, Tongtong Jiang, Zhiwei Wang, Jinhui Wang, Zeze Chen, Shuainan Li, Bingbing Fan, Peng Cui, Xing Zhao, Yingfeng Li, and Meicheng Li*

Cite This: *J. Phys. Chem. C* 2026, 130, 6973−6985

Read Online

ACCESS | Metrics & More | Article Recommendations | Supporting Information

ABSTRACT: Controlled-humidity annealing represents a powerful approach to modulate perovskite crystallization and film morphologies, as appropriate moisture facilitates the crystallization process. However, rapid crystallization during thermal annealing often produces randomly oriented films, introducing electronic heterogeneity that compromises the efficiency and stability of perovskite solar cells (PSCs). Herein, a moisture-modulated stepwise temperature annealing (MSTA) strategy is developed to enable good control over the crystallographic orientation of perovskite films, providing an alternative to film orientation regulation that is typically achieved with chemical additives or solvent chemistry engineering. Under varying humidity levels, distinct moisture-coordinated intermediate phases direct preferential (220) and (111) crystal orientations. MSTA-processed, (111)-oriented PSCs achieve a high efficiency of 25.38%, surpassing (220)-oriented counterparts (24.96%) while also demonstrating enhanced device longevity and comparable short-circuit current density. This work provides the potential of moisture-assisted, thermally mediated perovskite crystallization in governing film orientation, offering a promising pathway for air-processing perovskite films toward efficient and durable facet-dependent photovoltaics.



1. INTRODUCTION

With tunable bandgap, excellent charge carrier mobility, and long-range carrier diffusion, metal-halide perovskites have emerged as pivotal photovoltaic semiconductors enabling future energy technologies.[1,2] The performance of perovskite solar cells (PSCs) is closely linked to the crystal facets of the perovskite active layer, as atomic arrangement and facet coordination significantly influence carrier transport, surface energy levels, and stability of perovskites.[3] Studies have reported that while the (110) and (111) facets exhibit comparable optoelectronic properties, perovskites with a dominant (111) orientation demonstrate superior moisture tolerance compared to the (110)-oriented counterparts, owing to stronger H_2O adhesion on the (110) surface.[4] Therefore, perovskite films with preferential crystal orientations have attracted significant attention for fabricating high-quality PSCs. Solution processing is extensively utilized for fabricating perovskite films, owing to the good compatibility with perovskite precursors and the feasibility of fine-tuning solution properties.[5,6] However, controlling facet orientation in polycrystalline perovskite films deposited via spin coating remains a challenge due to rapid, uncontrolled crystallization. The resultant perovskite morphologies with disordered lattice orientations result in electronic heterogeneity with nonuniform charge transport and severe defect stacking, compromising both power conversion efficiency (PCE) and device stability.[7] Therefore, constructing perovskite film with a dominant crystalline orientation is crucial for promoting charge transfer in films and boosting the photovoltaic performance of PSCs. Strategies like epitaxial growth[8−10] and seed- or template-assisted crystallization[11−13] have successfully produced perovskite films with highly oriented facets, such as (100), (110), (111), and (200). Comparative studies consistently show that perovskite films with a preferred crystalline orientation deliver improved device performance and stability, demonstrating the critical role of oriented growth in advancing perovskite photovoltaics.

Controlling the microstructure of perovskite crystals involving intricate interactions among solvents, precursor components, additives, and intermediate phases can directly affect facet orientation and film morphology.[14] For instance, the synthesis of perovskite films with dominant (111)- and (100)-oriented facets has been achieved by incorporating

Received: March 8, 2026
Revised: May 5, 2026
Accepted: May 5, 2026
Published: May 13, 2026



Downloaded via INST OF CHEMISTRY on May 25, 2026 at 04:02:15 (UTC).
See https://pubs.acs.org/sharingguidelines for options on how to legitimately share published articles.

ACS Publications
© 2026 American Chemical Society

https://doi.org/10.1021/acs.jpcc.6c01538
J. Phys. Chem. C 2026, 130, 6973−6985

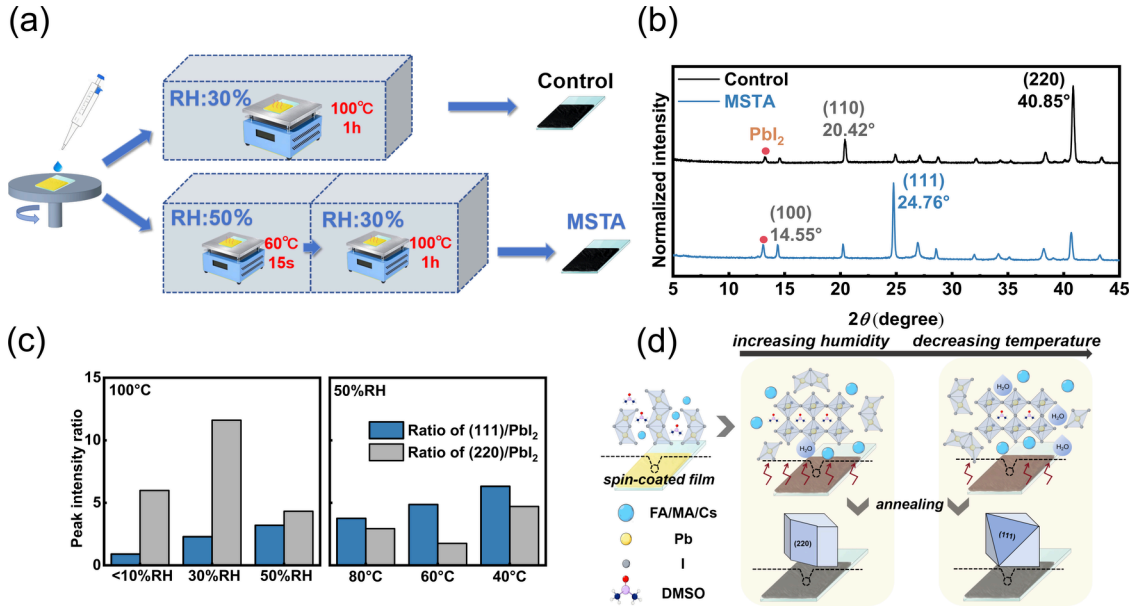


Figure 1. (a) Schematic illustration of the perovskite films treated with MSTA under ambient and controlled-humidity conditions. (b) XRD patterns of perovskite films under control and MSTA conditions. (c) Intensity ratios of perovskite (111) and (220) planes with respect to the PbI_2 peaks tracked over different humidity levels (left panel) and annealing temperatures (right panel), calculated from XRD patterns. (d) Schematic diagram illustrating the modulation of controlled crystalline orientation of perovskite films through moisture treatment and stepwise thermal annealing.

isomeric alcohol antisolvents (e.g., isopropanol and isobutanol) in a spin-coating process.[15−17] Alternatively, a ternary solvent mixture (*N*,*N*-dimethylformamide/dimethyl sulfoxide/*N*-methylpyrrolidone, DMF/DMSO/NMP) in place of conventional binary system was employed to modulate crystal facet orientation.[18] By leveraging the distinct coordination capabilities between the solvents and PbI_2, this approach directs intermediate phase formation and regulates growth kinetics, thereby promoting the preferential growth of (111)-oriented perovskite films. Component engineering also offers an effective pathway for controlling the crystal orientation of perovskites, such as by regulating the methylammonium/formamidinium (MA/FA) ratio to promote preferential crystal growth along the (001) plane.[19] In addition, extensive studies have devoted to achieving facet-specific growth through additive engineering. The introduction of surface-anchoring alkylamines can lower the surface energy of the (100) facet via alkylammonium ligand anchoring, making it thermodynamically favorable during crystallization.[20,21] Similarly, incorporating organic ammonium salts into the PbI_2 precursor solution has proven effective in promoting oriented perovskite growth along the (111) direction.[22] A variety of other additives, including N-heterocyclic compounds such as piperidine,[23] alkylphenanthroline,[24] bipyridyl,[25] and others[26,27] as well as amidino-based[28−30] and amine-containing[4,31] molecules, have also been employed to selectively direct the growth of specific facets such as (100) and (111) planes. However, many of structural residues from additives incorporated into perovskite films can render a potential threat to stability by introducing heterogeneous microstructures that act as carrier recombination or degradation sites. Therefore, developing alternative approaches to achieve preferential perovskite crystal growth during solution deposition remains an urgent need for realizing efficient PSCs.

Perovskite materials are highly sensitive to moisture, with excessive moisture leading to the loss of organic cations and collapse of the inorganic framework, ultimately degrading the performance of the perovskite films and devices.[32,33] To mitigate moisture-induced degradation, a range of additives have been incorporated into perovskite precursors. These include ionic liquids,[34] polymers,[35] and compounds containing hydrophobic moieties, such as alkyl ammonium halides,[36,37] guanidinium salt,[38] and acetamidinium salt.[39] Interestingly, however, controlled amounts of H_2O have also been shown to positively influence perovskite growth and crystallization for improving the photoelectric properties.[40−43] The introduction of H_2O alters the solution chemistry and can direct crystal growth orientation. Recent studies indicate that adding H_2O to the antisolvent promotes preferential growth along the (111) plane and refines surface morphology, attributing to the formed nucleation sites to strongly bind H_2O molecules for suppressing atomic assembly into (100) and (110) facets.[44] Additionally, a H_2O-rich solvent also facilitates the growth orientation of perovskite films.[45] Specifically, the formation of (100)-oriented $CsPbI_2Br$ films is enhanced through the desorption of DMSO from a flexible $PbI_2{\cdot}DMSO{\cdot}H_2O$ intermediate complex rather than from a more tightly coordinated $PbI_2{\cdot}DMSO$ phase. Notably, solution-processed metal-halide perovskite films typically require annealing under a humidity-controlled condition (relative humidity, RH = 30−40%), as appropriate moisture has been reported to be capable of facilitating perovskite crystallization.[46,47] Hence, it is quite interesting to investigate whether the cooperative effect of a certain humidity and the annealing treatment promotes preferential crystal orientation of the perovskites for improving device efficiency and stability. However, significant efforts have focused on understanding how humidity enhances crystallization of perovskite films or on using chemical additives to protect films from high humidity,[48,49] studies that explore humidity-modulated crystal orientation as an additive-free strategy to enhance perovskite film and device performance are crucial yet remain scarce.[50]

https://doi.org/10.1021/acs.jpcc.6c01538
J. Phys. Chem. C 2026, 130, 6973−6985

In this study, a moisture-modulated stepwise temperature annealing (MSTA) process was developed to control the crystal nucleation and growth of perovskite films. The MSTA process involves two distinct stages: initially annealing the spin-coated perovskite precursor film at a low temperature under controlled humidity in ambient air, followed by high-temperature annealing under a different specific humidity (Figure 1a). The stepwise thermal annealing coupled with controlled humidity enables facet-selective growth of perovskite films. However, to the best of our knowledge, the specific manipulation of perovskite film orientation through gradient/stepwise thermal annealing has not yet been reported, despite the technique being well established for improving perovskite film crystallization.[51,52] This approach promotes preferential film orientation along the (220) and (111) crystal planes without introducing facet orientation-related chemical additives, thereby facilitating the fabrication of facet-dependent PSCs. Devices fabricated with (111)-dominated perovskite films achieved a high PCE of 25.38%, accompanied by a superior open-circuit voltage (V_{OC}), a high fill factor (FF), and a comparable short-circuit current density (J_{SC}) relative to those of the (220)-dominated counterparts. Simultaneously, the resultant unencapsulated PSCs based on MSTA-derived (111)-oriented perovskite films also demonstrated improved long-term stability, partially attributable to the enhanced environmental resistance inherent to the (111)-oriented films. This work provides a promising pathway for fabricating high-quality, crystal-oriented perovskite films in advancing high-performance facet-dependent PSCs.

2. EXPERIMENTAL SECTION

2.1. Materials

All chemical reagents and solvents were purchased from commercial sources and used without further purification. $TiCl_4$ (purity: 99.9%) was purchased from Aladdin (Shanghai, China). Lead iodide (PbI_2, 99.999%), *N*,*N*-dimethylformamide (DMF, 99.9%), dimethyl sulfoxide (DMSO, 99.9%), chlorobenzene (CB, 99.9%), and acetonitrile (ACN, 99.99%), were obtained from Sigma-Aldrich. Formamidinium iodide (FAI, 99.8%), cesium iodide (CsI, 99.98%), methylammonium chloride (MACl, 99.99%), 2-phenylethylammonium hydroiodide (PEAI), *tert*-butylpyridine (tBP), libis(trifluoromethanesulfonyl)-imide (Li-TFSI, 99%), 2,2′,7,7′-tetrakis[*N*,*N*-di(4-methoxyphenyl)-amino]-9,9′-spirobifluorene (Spiro-OMeTAD, 99.99%), fullerene (C_{60}), and 2,9-dimethyl-4,7-diphenyl-1,10-phenanthroline (BCP) were purchased from Xi'an Yuri Solar Co., Ltd.

2.2. Device Fabrication

FTO/ETL Preparation. F-doped SnO_2 (FTO) substrates were ultrasonically cleaned sequentially with detergent, deionized water, ethanol, and deionized water for 15 min each. Prior to TiO_2 deposition, substrates underwent UV-ozone treatment for 30 min to achieve hydrophilic surfaces. The TiO_2 electron transport layer (ETL) was prepared by mixing titanium tetrachloride (4 mL) with deionized water (200 mL) under stirring to form a TiO_2 precursor solution. FTO substrates were then immersed in the 70 °C TiO_2 precursor bath for 40 min to deposit TiO_2 thin films. Subsequently, the TiO_2-coated substrates were rinsed sequentially with water−ethanol−water and scrubbed on the glass side with ethanol−water solution to maintain optical transparency. Before perovskite spin-coating, FTO/TiO_2 substrates received an additional 30 min UV-ozone treatment to enhance wettability.

Perovskite Layer Fabrication. A 1.54 M $FA_{0.85}MA_{0.1}Cs_{0.05}PbI_{2.85}Cl_{0.15}$ precursor solution was prepared by dissolving 224.4 mg FAI, 742.0 mg PbI_2, 10.1 mg MACl, and 19.8 mg CsI in mixed solvent of 1 mL DMF/DMSO (4:1 v/v). Perovskite films were fabricated via a one-step spin-coating process: In a N_2-filled glovebox, 37 μL of precursor solution was spin-coated onto FTO/TiO_2 substrates at 4000 rpm for 18 s, with 985 μL of diethyl ether dispensed as an antisolvent at approximately 6 s into the spin-coating process. The spin-coated wet films on FTO/TiO_2 substrates were then subjected to two distinct annealing protocols to obtain perovskite films: (i) Continuously annealing at constant humidity: the spin-coated films were annealed continuously at 100 °C for 1 h in a homemade humidity-controlled chamber (a schematic illustration of the chamber shown in Figure S1). Different relative humidity (RH) levels were tested (<10% RH, 30 ± 2% RH, 50 ± 2% RH, and 70 ± 2% RH). (ii) MSTA strategy: the spin-coated films were first annealed at lower temperature (40, 60, and 80 °C) under controlled humidity in an ambient-air environment until immediately prior to black perovskite phase formation. Subsequently, the resulting films underwent a second annealing step at high-temperature annealing of 100 °C under a fixed humidity of 30 ± 2% RH for 1 h.

Passivation Layer Deposition. A passivation solution was prepared by dissolving 4.5 mg of PEAI in 1 mL of anhydrous isopropanol (IPA). After perovskite film was cooled, the PEAI solution was spin-coated onto the perovskite layer at 4000 rpm for 30 s, followed by annealing at 100 °C for 3 min.

HTL Deposition. Spiro-OMeTAD was chosen as the hole transport layer (HTL) due to its suitable valence band position and solution processability. The Spiro-OMeTAD solution was prepared by dissolving 72.3 mg of Spiro-OMeTAD, 26.6 μL of tBP, and 18 μL of Li-TFSI solution (520 mg mL^{-1} in ACN) in 1 mL of CB. After deposition and cooling of the passivation layer, the Spiro-OMeTAD solution was spin-coated at 4000 rpm for 30 s onto the PEAI layer.

Counter Electrode Fabrication. A gold electrode with thickness of 60 nm was deposited onto the Spiro-OMeTAD layer by thermal evaporation under a vacuum of approximately 4×10^{-4} Pa at a speed of 0.5 Å s^{-1} to complete the fabrication of PSC.

2.3. Film and Device Characterization

The morphology of the perovskite films was characterized using field-emission scanning electron microscopy (SEM, Hitachi S-4800) and atomic force microscopy (AFM, FM-Nanoview 1000). Surface potential mapping was performed using Kelvin probe force microscopy (KPFM). The film crystallinity was analyzed by X-ray diffraction (XRD, D8 Advance Bruker). Optical absorbance spectra were recorded with a UV−vis spectrophotometer (UV-2600). Steady-state photoluminescence (PL) spectra were acquired using an FLS980 fluorescence spectrometer under 405 nm excitation. Carrier behavior within perovskite films was investigated through time-resolved photoluminescence (TRPL, FLS980). In situ PL spectra were collected using the FLS980 system with 405 nm excitation light (Lanhai Science Instrument RS-232). The surface chemical environment of the perovskite film was examined with X-ray photoelectron spectroscopy (XPS, Thermo Fisher Scientific ESCALAB 250Xi). Electrochemical impedance spectroscopy (EIS) and Mott−Schottky analysis were carried out using an impedance analyzer (Hioki IM3570). For Mott−Schottky analysis, capacitance−voltage ($C-V$) measurements were performed by sweeping the applied voltage from 0 to 1.5 V at a fixed frequency of 1 kHz with an AC amplitude of 50 mV.

The current density−voltage ($J-V$) scanning was performed under simulated AM1.5 G illumination (100 mW·cm^{-2}) produced from a xenon lamp solar simulator, calibrated with a certified Si reference cell from the National Institute of Metrology. $J-V$ curves were recorded using a Keithley 2400 with a scanning speed of 0.06 V·s^{-1} (−0.1 to 1.3 V). The device active area, defined by a shadow mask, was determined to be 0.076 cm^2. The external quantum efficiency (EQE), dark $J-V$ measurements for control, and MSTA-derived devices were performed with an Enli Tech QE-R system under AC modulation.

3. RESULTS AND DISCUSSION

$FA_{0.85}MA_{0.1}Cs_{0.05}PbI_{2.85}Cl_{0.15}$ perovskites with mixed A-site cations and halides prepared using a one-step spin-coating process were employed to study crystal orientation modulation

https://doi.org/10.1021/acs.jpcc.6c01538
J. Phys. Chem. C 2026, 130, 6973−6985

induced by MSTA. The ambient temperature throughout the entire annealing process was maintained at 19 ± 1 °C to prevent ambient temperature fluctuations from affecting absolute humidity. The methods for creating different humidity conditions are shown in Figure S1 (Supporting Information). Usually, the appropriate humidity at 30−40% RH was reported to be conducive to the ambient annealing of perovskite films for improving crystal growth and film morphology.[48,53] First, the spin-coated perovskite films continuously annealed at different RH levels were conducted for 1 h (Figure S2a, Supporting Information). X-ray diffraction (XRD) measurements were performed to study the crystallinity of the perovskite films. Three dominant diffraction peaks at 20.42, 24.67, and 40.85°, corresponding to the (110), (111), and (220) planes of the α-perovskite phase, respectively,[54] were observed. In addition, a tiny peak at a 2θ value of 13.22°, which is assigned to PbI_2, was also observed in the XRD pattern. Interestingly, when perovskite films were thermally annealed at 100 °C with controlled humidity (~30% RH), a prominent peak of (220) plane with relatively high intensity was observed (Figure 1b, top panel, denoted as the control film), indicating the formation of a distinct preferred crystal orientation in the perovskite films. Increasing the RH values during the annealing to ~50% was found to compromise the preferred (220) crystal orientation of the perovskite film, as indicated by an increased (111) peak and the emergence of additional minor phases. A further increase to ~70% RH results in a strong PbI_2 peak, indicating either incomplete perovskite phase formation or film decomposition. Similarly, reduced humidity (<10% RH) is also detrimental to crystallization quality of perovskite films (Figure S2c, Supporting Information). Notably, XRD spectra demonstrated that the perovskite film treated with continuous annealing at ~50% RH exhibited a stronger (111)-related peak compared to the film annealed at ~30% RH (see Figure S3 for XRD patterns of films subjected to continuous annealing at ~50% RH and 60 °C). These results suggest that crystal orientation can be regulated by employing the MSTA approach through modulating humidity and temperature.

The spin-coated perovskite films under MSTA treatment involved an initial annealing step at 100 °C under varying RH levels for duration time of 15 s, followed by a main annealing step at 100 °C for 1 h under a fixed ~30% RH. Subsequently, to further control the orientation of perovskite films, the initial annealing temperature at ~50% RH was lowered (Figure S2b, Supporting Information). A corresponding increase in the relative intensity of the (111) peak was observed with decreasing temperature. When the temperature reached 60 °C in the initial annealing step, the XRD pattern was dominated by the (111) peak, with the (220) and (110) peaks being largely suppressed (Figure 1b, bottom panel, denoted as the MSTA film). These results indicate that both dominant (220) and (111) facet orientation in perovskite films can be selectively obtained by the MSTA strategy (annealing duration-dependent XRD patterns shown in Figure S4, Supporting Information). Analysis of the XRD intensity ratios of (111) and (220) diffraction peaks relative to the PbI_2 peak further confirms this orientation regulation. The perovskite film treated with MSTA at 100 °C and ~30% RH exhibited a maximum (220)/PbI_2 ratio (Figure 1c, left panel), corresponding to a dominant (220)-facet orientation. As the initial annealing temperature decreased under controlled humidity of ~50% RH, the (111)/PbI_2 ratio progressively increased while the (220)/PbI_2 ratio decreased (Figure 1c, right panel), achieving a predominant (111) orientation at an initial annealing step of 60 °C (Figure 1a, dependence of the (111)/(220) diffraction intensity of MSTA-processed perovskite films on annealing temperatures and RH levels shown in Figure S5, Supporting Information). These results clearly indicate that the facet orientation of $FA_{0.85}MA_{0.1}Cs_{0.05}PbI_{2.85}Cl_{0.15}$ can be regulated from dominant (220) orientation to a preferred orientation along (111) plane using the MSTA approach. Comparative studies have shown that the (111) crystal facet of perovskite film exhibits similar optical properties with the (100)- and (110)-oriented crystals but possesses superior hydrophobicity and charge transport properties.[55] In this study, perovskite films with (220) and (111) orientations were successfully obtained, providing an opportunity for investigation into correlation between the relevant facet-dependent electronic properties and the performance of devices.

XRD patterns revealed that the MSTA-modified film with (111) orientation exhibited improved crystallinity compared to the (220)-oriented counterparts, as indicated by a reduction in the full width at half-maximum (fwhm) value (Figure S2c, Supporting Information). Additionally, shifts in the XRD characteristic peaks corresponding to the (220) and (111) crystal planes under varying humidity levels suggest that the moisture influences the distortion of the perovskite structure (Figure S2c, Supporting Information). Figure S6 (Supporting Information) illustrates the color evolution routes of the MSTA-modulated perovskite films observed from the initial annealing step. Compared to the control film annealed at 100 °C and ~30% RH, which rapidly turned black within 8 s, the MSTA film processed at 60 °C and ~50% RH exhibited a relatively slower color change, remaining brown over the same period. This delayed color change, corresponding to a prolonged phase-transition process, underscores the role of the MSTA in modulating crystallization kinetics to facet orientation under different humidity and temperature conditions. The mechanism underlying the preferred facet orientation induced by the MSTA strategy can be attributed to combined influence of moisture and annealing temperature (Figure 1d). During the initial annealing of the spin-coated perovskite liquid/crystallization phase in ambient air, moisture permeates the film and promotes crystallization by forming H_2O-involved intermediate complexes.[45] The low-temperature annealing step slows down the solvent evaporation both in the bulk and on the surface of the film, extending the nucleation time for perovskites and providing a buffer for the rapid crystallization of perovskite grains (Figure S6, Supporting Information). The subsequent high-temperature annealing step facilitates the removal of residual solvents and thermodynamically drives crystallization toward completion. The moisture present at varying humidity levels promotes the formation of distinct H_2O-involved intermediates, which subsequently guide the preferential growth of perovskite films toward favorable crystal planes. By extending the nucleation time window, the MSTA process enables the formation of favorable crystal nuclei, resulting in fabrication of a perovskite film with a controlled crystalline orientation.

In situ photoluminescence (PL) spectroscopy was employed to investigate the crystallization kinetics of perovskite films processed with the MSTA strategy. To understand the crystallization process during the initial annealing stage of MSTA, which leads to preferential (220) and (111) facet

https://doi.org/10.1021/acs.jpcc.6c01538
J. Phys. Chem. C 2026, 130, 6973−6985

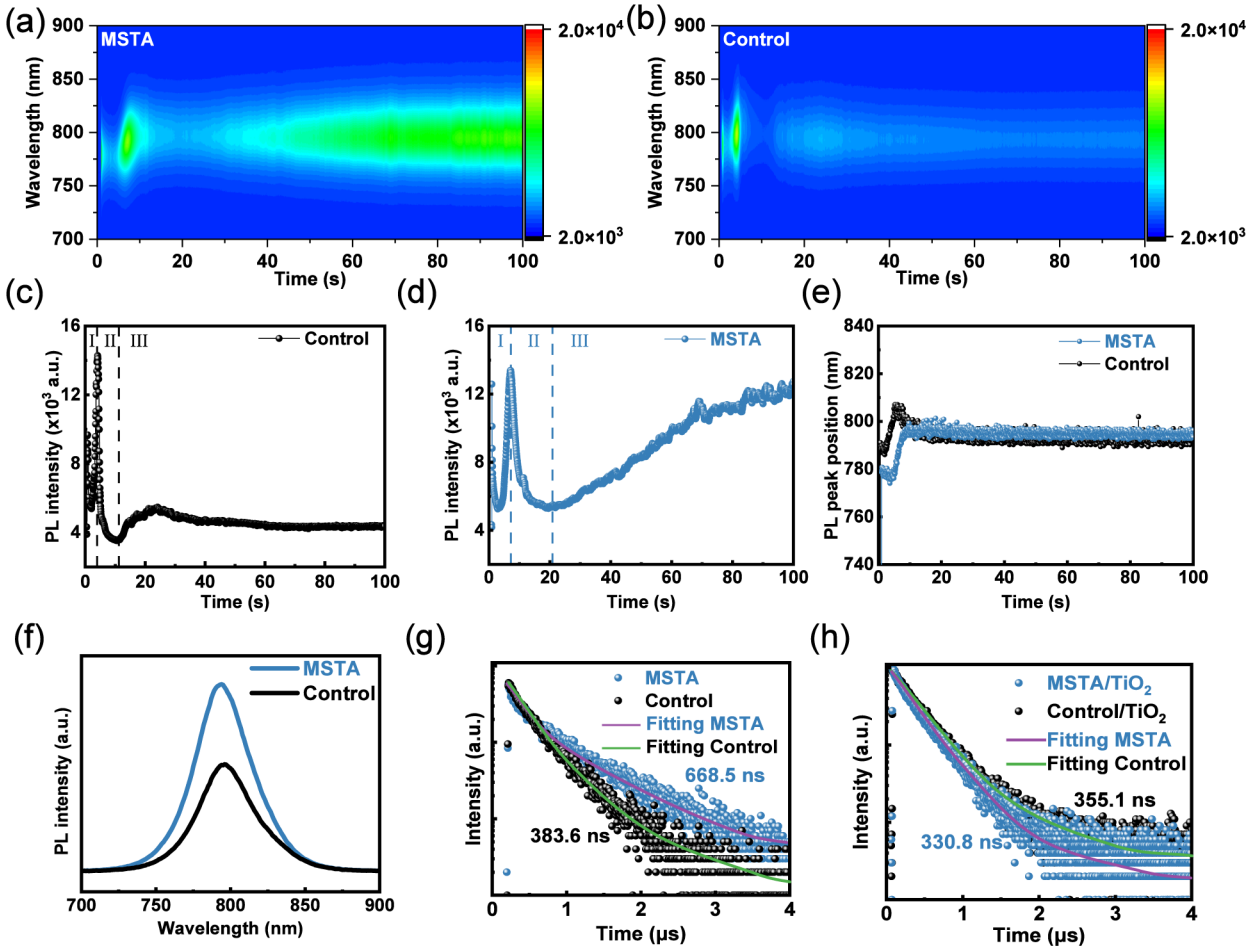


Figure 2. 2D contour maps of in situ PL spectra of the (a) control and (b) MSTA-treated films. Evolution of (c, d) the PL intensity and (e) the peak position for the control and MSTA-treated films, with data extracted from panels (a) and (b), respectively. (f) Steady-state and (g, h) time-resolved PL spectra of the control and MSTA-treated perovskite films. The time-resolved PL data were presented without and with TiO_2 ETL layers.

orientation, two sets of the spin-coated perovskite films were processed: one annealed at 100 °C and ∼30% RH (labeled as "control"), and the other treated at 60 °C and ∼50% RH (labeled as "MSTA"). The corresponding in situ PL results were presented as 2D contour plots in Figure 2a,b. The "0 s" in the *x*-axis represented the time for beginning thermal annealing of spin-coated perovskite films after dripping the antisolvent (diethyl ether). After annealing, the PL signals nearly instantly appeared at 770−790 nm. The annealing process can be divided into three distinct stages according the in situ PL. Stage I—rapid crystallization: Thermal annealing triggered accelerated crystallization, accompanied by a rapid increase in PL intensity.[29] The control and MSTA-treated films reached their first emission peaks at approximately 4 and 7 s, respectively (Figure 2c,d). The slower increase of the PL intensity in the MSTA film suggests that the combined effect of elevated moisture and reduced annealing temperature effectively retards the conversion from solvent complex to perovskite crystal phases. This behavior may be associated with the distinct intermediate phases that involve moisture. Additionally, the MSTA film displayed a lower PL intensity at the peak position during the initial annealing stage, suggesting reduced nucleation density within films. Stage II—dissolution: Under prolonged thermal annealing, both films experienced rapid PL quenching after reaching the peak position, which was associated with the dissolution of perovskite crystals on the film surface as the residual solvent evaporated from bulk films.[29,56] Notably, the decay times to the minimum peak intensity were approximately 6 s for the control film and 13 s for the MSTA film, indicating a reduced evaporation rate of solvents within MSTA-treated film. Stage III—recrystallization: Continued solvent volatilization drives further crystallization and grain coarsening, as indicated by the progressive recovery of PL intensity. While the control film showed a steep initial rise in PL intensity at the beginning of stage III, the MSTA-processed film displayed a more gradual increase, corresponding to an extended crystallization time window. This prolonged duration provides a broader growth window for the perovskite crystals on the surface to develop preferential orientation, leading to a dominant crystalline alignment along the (111) plane. It is noteworthy that continued thermal annealing led to PL quenching in the control film. This effect can be attributed to the continuously increasing Urbäch energy, a typical phenomenon that indicates the gradual formation of defects in the perovskite microstructure.[48] Corresponding optical images of spin-coated films taken at various treatment durations during thermal annealing under control and MSTA conditions revealed that, compared to the control film, the MSTA precursor film required a prolonged duration to achieve a comparable level of black

https://doi.org/10.1021/acs.jpcc.6c01538
J. Phys. Chem. C 2026, 130, 6973−6985

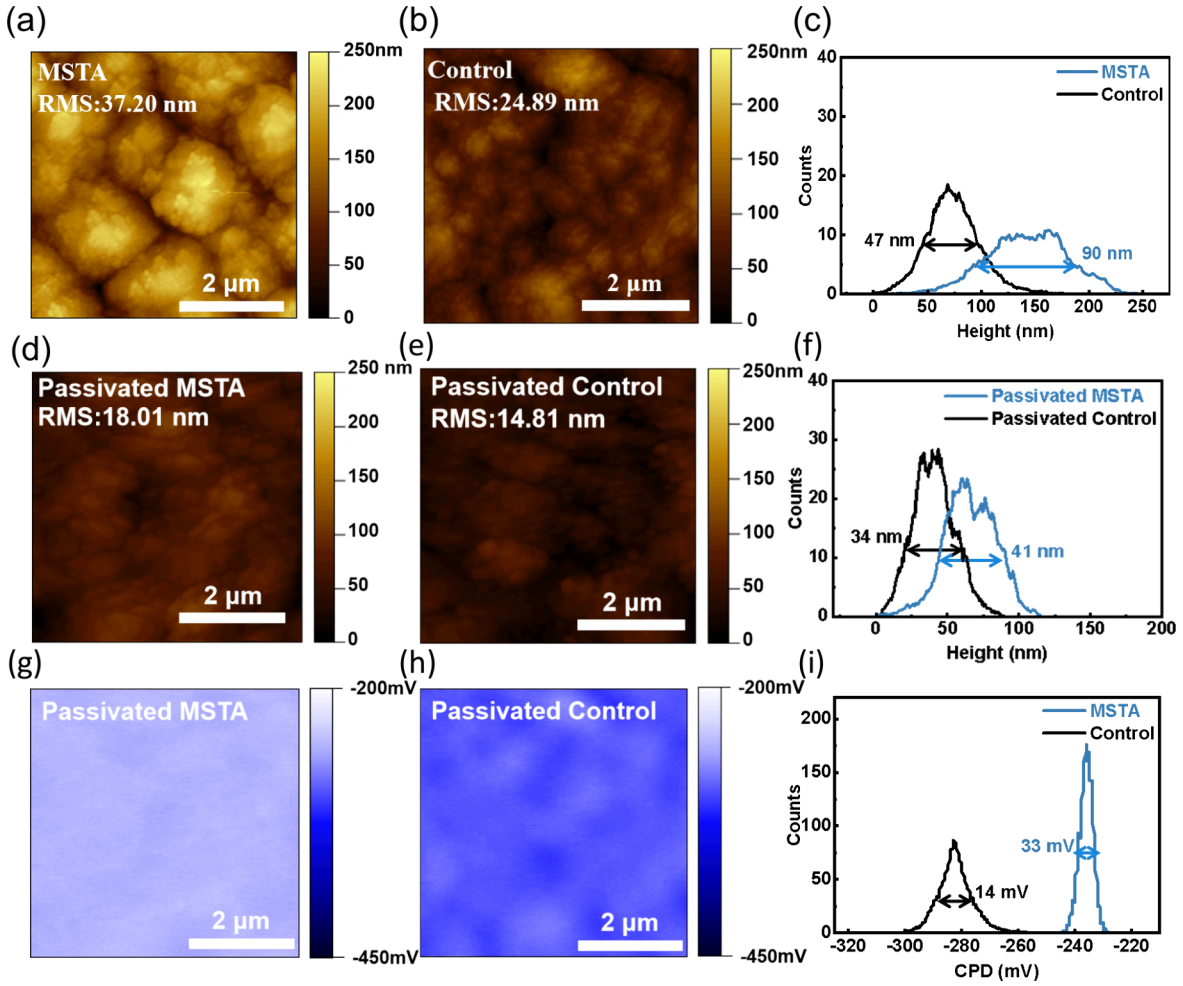


Figure 3. AFM images of perovskite films before and after treatment with a PEAI passivator, both (a, d) with and (b, e) without MSTA processing. The height distribution on the corresponding AFM images of perovskite films (c) before and after (f) PEAI treatment. KPFM images of PEAI-passivated perovskite films treated (g) with and (h) without MSTA processing and the corresponding (i) surface potential distributions. The fwhm values of the distribution profiles are highlighted in (c, f, i).

coloration (Figure S7, Supporting Information). Thus, MSTA processing modulates the nucleation kinetics and retards the crystal growth of perovskite film, facilitating the formation of high-quality perovskite films with large grain sizes.

Furthermore, during the first few seconds following thermal annealing, the evolution of the PL peak positions differed between the two films, as plotted in Figure 2e. A sharp red shift toward a long wavelength (around 790 nm) in the PL peaks was observed within the initial 10 s for both the control and MSTA films. This rapid shift is interpreted as the growth of perovskite clusters and accelerated crystallization in the residual solvent matrix.[57] The full transition to the perovskite bulk phase in the MSTA-treated film was completed at 10.0 s, as opposed to 6.5 s for the control film. This likely stems from the slowly rising precursor concentration caused by solvent evaporation under reduced annealing temperature and retarded intermolecular exchange process in the MSTA film.[58] Moreover, a distinct blue shift (~11 nm) in the PL peak position was detected within 10 s in the MSTA film compared to the control film. This suggests the presence of distinct moisture-coordinated intermediate phases during the early stage of thermal annealing, which are associated with ambient humidity levels and involved in the conversion from perovskite nuclei to bulk phases. It should be noted that upon continued thermal annealing, the PL peaks for both films red-shifted and plateaued at nearly identical positions. This suggests that the perovskites in both films share a very similar crystal structure, differing primarily in their orientation planes, which was supported with XRD results. Steady-state PL further corroborated these findings. As shown in Figure 2f, the MSTA-treated film deposited on the FTO substrate exhibited significantly stronger PL emission intensities with negligible spectral blue-shift compared to the control film, demonstrating a substantial suppression of nonradiative recombination. This can be ascribed to the retarded crystallization process induced by the MSTA strategy, which promotes preferred crystalline orientation and defect reduction in the modified perovskite film. Meanwhile, time-resolved PL (TRPL) spectra showed a similar trend, as shown in Figure 2g and Table S1 (Supporting Information). Fitting the TRPL spectra by using a biexponential decay model function yielded a significant prolongation of the average PL lifetime (τ_{ave}) from 383.6 ns for control film to 668.5 ns for the MSTA-treated counterpart. This prolonged τ_{ave} indicates that the MSTA strategy promotes the crystallinity and preferred orientation of the perovskite film, prolonging charge carrier lifetime and reducing trap-assisted recombination. In addition, PL quenching experiments on FTO/TiO_2 substrates exhibited a faster lifetime decay (τ_{ave}

https://doi.org/10.1021/acs.jpcc.6c01538
J. Phys. Chem. C 2026, 130, 6973−6985

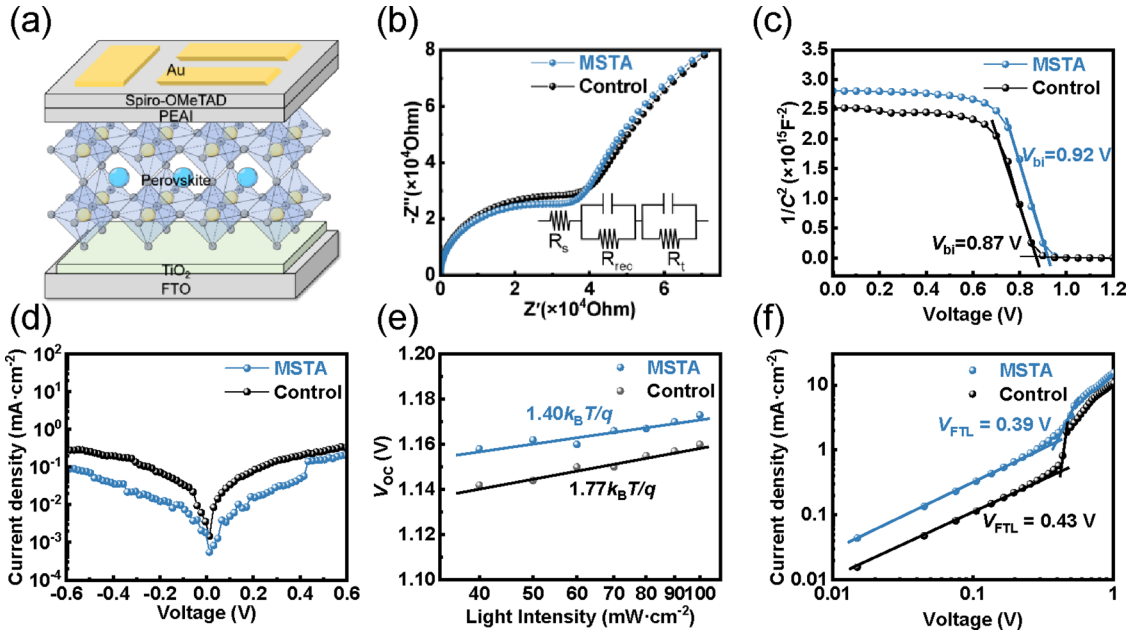


Figure 4. (a) Schematic illustration of device structure of the normal PSCs. (b) Nyquist plots of the control and MSTA-treated PSCs (inset: equivalent circuit). (c) Mott−Schottky plots of the devices with and without MSTA processing. (d) Dark $J-V$ curves of the corresponding devices. (e) V_{OC} values dependent on the illumination light intensity for the control and MSTA-treated devices. (f) Dark $J-V$ curves measured by the SCLC method based on the electron-only devices with FTO/TiO_2/perovskite/C_{60}/BCP/Ag configuration, where BCP is bathocuproine.

= 330.8 ns) for the MSTA-treated film compared to the control film (τ_{ave} = 355.1 ns), as shown in Figure 2h. This faster quenching implies a more productive charge extraction and transfer process at the modified perovskite film/ETL interface, which may be attributed to more favorable band alignment and a reduction in interfacial defects.[59]

Scanning electron microscopy (SEM) and atomic force microscopy (AFM) were performed to evaluate the effect of MSTA process on the morphological quality of the perovskite films. Top-view SEM images revealed that both the MSTA and control films were fully covered with polycrystalline perovskites and exhibited compact surface morphology (Figure S8, Supporting Information). Statistical analysis of grain-size distributions indicated that the average crystal size of the MSTA-processed film was approximately 520 nm, which was 1.3 times larger than that of the control counterpart. This increase can be attributed to the slow solvent evaporation during the initial low-temperature annealing stage, which provided an extended time window for perovskite grain growth and fusion. As a result, perovskite film with large grain sizes was formed, as corroborated by the narrower XRD peak (Figure 1b, Figure S2c, Supporting Information) and higher PL intensity (Figure 2f). Moreover, the surface roughness of the perovskite films was characterized using AFM images (Figure 3a−c). The root-mean-square (RMS) roughness values for the control and MSTA films were 24.89 and 37.20 nm, respectively. The AFM results indicate the MSTA treatment would increase the roughness of the perovskite film. This degradation of the perovskite film surface is likely attributable to the moisture-induced surface erosion during the initial high-humidity exposure in MSTA process. Generally, phenethylammonium iodide (PEAI) is commonly utilized to improve PSC performance due to its ability to passivate interfacial defects and modulate surface energy levels.[60] Spin-coating a thin PEAI layer above the perovskite layer enables the minimization of interfacial recombination losses.[61] Here, a PEAI interlayer was introduced between the perovskite and HTL to enhance charge transport and extraction. Interestingly, after PEAI interfacial passivation, AFM characterization revealed a reduction in surface roughness, with surface RMS roughness decreasing to 14.81 and 18.01 nm for the control and MSTA films, respectively, along with a narrower height distribution of passivated films treated with MSTA compared to the control counterpart (Figure 3d−f). The cross-sectional SEM images showed well-connected perovskite crystals in both control and MSTA-treated films with no noticeable difference in surface coverage by HTL (Figure S9, Supporting Information). These results are consistent with favorable interfacial contact between the perovskite and HTL layers, which correlates with the passivation efficacy of PEAI in MSTA-processed perovskite films. The effectiveness of PEAI passivation on the perovskite film surface may be related to the penetration of passivator into the perovskite grains and surface wrinkles of the MSTA-treated perovskite films. Therefore, the PEAI layer was specifically engineered to optimize the perovskite/HTL interface.

Furthermore, kelvin probe force microscopy (KPFM) measurements demonstrated a similar result that the MSTA treatment led to a more nonuniform potential distribution across the perovskite film surface compared to the control case, as further evidenced by a significantly broader profile of surface contact potential difference (CPD) distribution of MSTA film (Figure S10, Supporting Information). In contrast, following PEAI interfacial passivation, the perovskite films showed distinct variation trends in the surface potential distribution between the control and MSTA films (Figure 3g−i). The MSTA-derived film exhibited a significantly narrower and more uniform potential distribution compared to the control film. This improved homogeneity is likely attributable to enhanced interfacial contact between the moisture-eroded perovskite layer and the PEAI passivator. Furthermore, the MSTA-derived passivated perovskite surface exhibited a higher

https://doi.org/10.1021/acs.jpcc.6c01538
J. Phys. Chem. C 2026, 130, 6973−6985

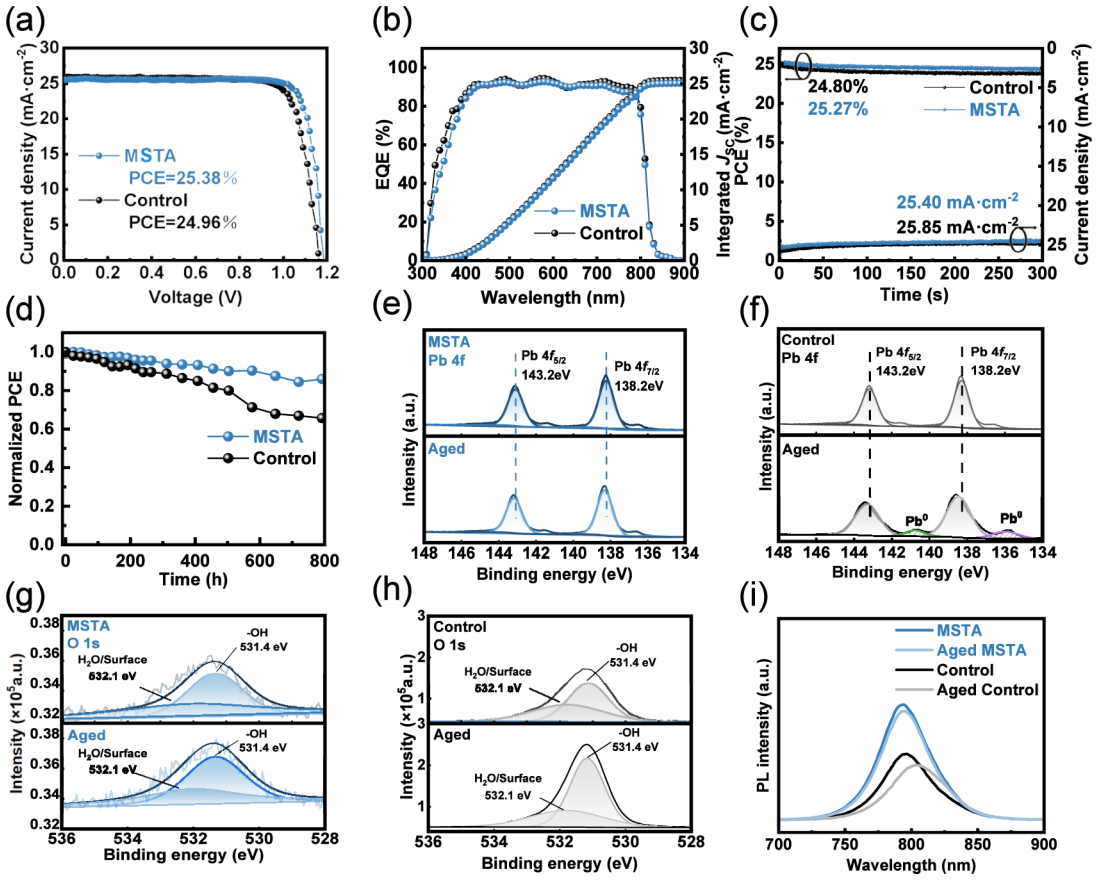


Figure 5. (a) $J-V$ curves of the control and MSTA-treated devices by reverse scanning under AM 1.5G illumination (100 mW cm^{-2}). The active area of the device is ∼0.08 cm^2. (b) EQE spectra and corresponding integrated J_{SC} of the PSCs derived with control and MSTA-treated films. (c) Steady-state photocurrent and PCE measured at maximum power point under constant light illumination for the control and MSTA-treated devices. (d) Normalized PCE evolution of unencapsulated devices after storage at 20 ± 2 °C in ambient air with 15−20% RH. Pb 4f XPS spectra of the (e) MSTA-treated and (f) control films, recorded before and after 7 days of aging under ambient conditions (20 ± 2 °C, ∼30% RH). O 1s XPS spectra of the corresponding (g) MSTA-treated and (h) control films, collected before and after aging under identical conditions. (i) PL stability of both films evaluated before and after aging at the same conditions.

average surface CPD of −236 mV, which is approximately 50 mV higher than that of the passivated control counterpart (Figure 3i). The slightly elevated surface potential facilitates hole transport and simultaneously impedes electron transport at the perovskite/HTL interface, thereby improving charge extraction efficiency.[62]

After fabricating perovskite films with well-defined (220)- and (111)-facet orientation, the photoelectric characteristics of the perovskite films and the corresponding PSCs with the planar device architecture illustrated in Figure 4a were evaluated. Electrochemical impedance spectroscopy (EIS) was performed to study the interfacial charge transport and recombination behavior in PSCs dominated by different crystal facets (Figure 4b). The Nyquist plots displayed two distinct arcs, corresponding to the charge transport resistance (R_{ct}) in the high-frequency region and the charge recombination resistance (R_{rec}) in the low-frequency region, respectively.[63] By fitting the resulting plots with an equivalent circuit model (inset of Figure 4b, fitted values summarized in Table S2, Supporting Information), the MSTA-derived device exhibited a reduction in R_{ct} (R_{ct} = 3.9 × 10^4 Ω) and an increase in R_{rec} (R_{rec} = 2.2 × 10^5 Ω) compared to the control one (R_{ct} = 2.2 × 10^5 Ω, R_{rec} = 4.1 × 10^4 Ω). These results indicate that the MSTA-based device with (111)-facet domination offered better interfacial contact, enhanced charge transfer, and suppressed nonradiative recombination, thus presenting higher V_{OC} and FF.[64] Capacity and voltage plots (Mott−Schottky analysis) were measured to analyze the built-in potential (V_{bi}) in PSCs (Figure 4c). The calculated V_{bi} value of the control device was 0.87 V, whereas the V_{bi} of the MSTA-treated one was 0.92 V. The increase in V_{bi} is beneficial for charge carrier separation/extraction and inhibiting the interface energy loss. Moreover, dark $J-V$ curves were conducted to assess the trap-state density and carrier recombination level in the PSCs by measuring leakage current. The MSTA-processed device possessed a lower saturation current density (J_0) compared with the control device (Figure 4d), demonstrating that photogenerated charges transfer more effectively through the transport layers with minimal shunt pathways. This reduction in J_0 observed in the MSTA device correlates with enhanced shunt resistance, suppressed carrier recombination, and improved charge extraction efficiency.[65] Furthermore, the dependence of V_{OC} on light intensity of PSCs was surveyed (Figure 4e). The slopes for the control and MSTA-processed devices were found to be 1.77 k_BT/q and 1.40 k_BT/q, respectively, indicating a reduction in the nonradiative recombination and trap-state density in the (111)-facet-oriented perovskite films.

Space-charge-limited current (SCLC) measurements were performed to further quantify the defect density (N_{trap}) of

https://doi.org/10.1021/acs.jpcc.6c01538
J. Phys. Chem. C 2026, 130, 6973−6985

perovskite films dominated with (220) and (111) facets. The current density−voltage ($J-V$) curves on electron-only devices structured as FTO/TiO_2/Perovskite/C_{60}/BCP/Ag were carried out under darkness, exhibiting characteristic ohmic and trap-filled limited (TFL) regions at low and intermediate bias, respectively (Figure 4f). Linear fitting of the ohmic and TFL regions yielded the trap-filling limited voltage (V_{TFL}) at their intersection, which correlates directly with N_{trap} (the calculation details presented in the Supporting Information). The MSTA-treated, (111)-oriented perovskite film exhibited a lower V_{TFL} (0.39 V) than the control film (0.43 V), with corresponding N_{trap} values decreasing from 3.59×10^{15} cm^{-3} for the control to 3.26×10^{15} cm^{-3} for the MSTA-treated film. This reduction in N_{trap} confirms that MSTA processing led to a decrease in trap-state density in (111)-facet-oriented perovskite films, consistent with the PL results (Figure 2f−h) and highlighting its potential in enhancing the FF and stability of PSC.[66]

Given the above properties of the perovskite films with different orientations, PSCs with a device configuration of FTO/TiO_2/Perovskite/PEAI/Spiro-OMeTAD/Au (Figure 4a), where Spiro-OMeTAD denotes 2,2′,7,7′-tetrakis[*N*,*N*-di(4-methoxyphenyl)amino]-9,9′-spirobifluorene, have been further fabricated for comparing the corresponding photovoltaic performance. The statistical photovoltaic parameters based on 20 devices showed that the control PSCs with a dominant (220) orientation exhibited an average PCE of 24.08 ± 0.60%. The MSTA-treated devices with a preferred (111) orientation boosted to 24.77 ± 0.47%, with the best PCE exceeding 25% (Figure S11 and Table S3, detailed photovoltaic parameters are shown in Table S4, Supporting Information). The MSTA-treated perovskite devices demonstrated a champion reverse scan of efficiency of 25.38% (Figure 5a), accompanied by a J_{SC} of 25.54 mA cm^{-2}, a V_{OC} of 1.19 V, and an FF of 83.8%. In contrast, the control counterpart achieved a lower PCE of 24.96%, with a J_{SC} of 26.13 mA cm^{-2}, a V_{OC} of 1.16 V, and an FF of 82.3%. MSTA processing modulated the crystallization process, and evidently enhanced the perovskite crystallinity and interfacial contact. This thereby results in enhanced band alignment (detailed analysis about the energy level alignment of control and MSTA-treated perovskite films is given in Figures S12 and S13, Supporting Information) and reduced current leakage, ultimately contributing to enhancements in V_{OC}, FF, and PCE in (111)-facet-oriented devices.[67] Moreover, MSTA-treated devices demonstrated a significantly suppressed hysteresis in comparison to the control devices (Figure S14, Supporting Information), which is due to the reduced interfacial defects and suppression of ion migration in (111)-dominated devices.[68]

To ensure the reliability of $J-V$ measurements, the external quantum efficiency (EQE) spectra were recorded across the 300−900 nm range, as shown in Figure 5b. The integrated J_{SC} were calculated to be 25.47 and 25.04 mA cm^{-2} for the control and MSTA-treated devices, respectively, in accordance with the J_{SC} values extracted from the $J-V$ measurements. Moreover, the stabilized power output (SPO) of the PSCs were conducted at maximum power point (MPP) by applying a constant bias voltage for 300 s (Figure 5c). The results indicate that PSCs with MSTA processing delivered the stabilized PCE of 25.27% and output current density of 25.40 mA cm^{-2} and exhibited a more stable power compared to the control device (24.80% of PCE, 25.85 mA cm^{-2} of J_{SC}), confirming the reliability of $J-V$ measurements. It is noteworthy that the control and MSTA-derived PSCs exhibited comparable J_{SC}, which aligned well with the nearly identical absorption intensities observed in the UV−vis absorption spectra (Figure S12, Supporting Information).

The effect of facet orientation on the long-term stability of unencapsulated perovskite devices was evaluated by exposure to an air atmosphere at 15−20% RH and 20 ± 2 °C. As shown in Figure 5d, the MSTA-treated device with (111) orientation maintained ∼85% of its original PCE over 800 h, whereas the PCE of the control, (220)-oriented device decreased to ∼65% of its initial efficiency. The long-term stability demonstrates that the (111) orientation is more stable. The enhanced stability originates from the intrinsic properties of the (111) facet, which features a closely packed atomic arrangement with higher bond energies, rendering it more resistant to moisture-induced degradation.[22,25] It is noteworthy that Table S5 (Supporting Information) demonstrated that the main parameter leading to the PCE dropping in MSTA-processed PSCs was FF. In addition, the facet-dependent robustness of perovskite films to resist latent damage was studied to gain insight into the corresponding PSC ambient stability. X-ray photoelectron spectroscopy (XPS) was used to analyze the surface composition and chemical changes during the aging process. The two characteristic peaks at 143.2 and 138.2 eV, corresponding to Pb $4f_{5/2}$ and $4f_{7/2}$ orbitals, respectively, exhibited a shift toward higher binding energies for control perovskite films after aging for 7 days under ambient conditions (20 ± 2 °C, ∼30% RH) (Figure 5f). Concurrently, two shoulder peaks belonging to metallic Pb (Pb^0) emerged at 140.8 and 136.0 eV in the aged film. These spectral changes are indicative of perovskite film decomposition during the aging process. Nevertheless, negligible signals of Pb^0 were detected in the aged MSTA-treated perovskite film, accompanied by no appreciable shift observed in the corresponding Pb 4f orbital peaks under ambient aging conditions (Figure 5e). Furthermore, compared to the control film, the O 1s characteristic peaks representing −OH (∼531.4 eV) and H_2O/surface (∼532.1 eV) adsorbed from ambient moisture[69] showed significant lower intensities in the MSTA-treated film (Figure 5g,h; for details regarding the contribution of the C═O group from the DMSO solvent, refer to Figure S15, Supporting Information), implying that the (111)-dominated perovskite surface is able to efficiently minimize interactions with moisture that induces perovskite degradation.[41] The reduced susceptibility to ambient moisture is further supported by the smaller increase in O 1s signals observed in the MSTA-treated film after aging, confirming the enhanced environment stability of the (111)-oriented perovskite surface. Steady-state PL measurements were performed on perovskite films before and after aging. The exposed control (220)-oriented perovskite film exhibited a decrease in the intensity of PL emission, accompanied by a clear red shift of the PL peak position during the aging process. In contrast, the exposed MSTA-treated, (111)-oriented film effectively mitigated this degradation, as evidenced by maintaining nearly identical peak position and minimal variation in PL intensity throughout the aging (Figure 5i). The enhanced stability of the (111)-oriented film is attributed to its superior film quality, as evidenced by water contact angle measurements (Figure S16, Supporting Information). This hydrophobicity prevents moisture from attacking the (111)-oriented perovskite, thereby inhibiting unfavorable phase transitions and stabilizing the black phase. These results demonstrate that MSTA-treated perovskite films,

https://doi.org/10.1021/acs.jpcc.6c01538
J. Phys. Chem. C 2026, 130, 6973−6985

which exhibit a dominant (111) orientation, achieve high efficiency and ambient stability, highlighting the potential of the controllable, additive-free MSTA process to modulate preferred perovskite facet orientation for advancing high-performance and stable PSCs.

4. CONCLUSIONS

In summary, perovskite films exhibiting dominant (220) and (111) facet orientations have been fabricated using a simple, and additive-free MSTA strategy. By integrating stepwise thermal annealing with humidity control, the processes of solvent evaporation and moisture-assisted crystallization were regulated, allowing modulation of the nucleation time window and buffering the rapid crystallization of perovskite grains, enabling control over the films with different preferential crystal orientations. The resulting (111)-oriented PSCs achieved an impressive PCE of 25.38%, surpassing the 24.96% efficiency for the (220)-oriented counterparts while also demonstrating an enhanced device longevity and a comparable J_{SC}. This work highlights the effectiveness of moisture-assisted, thermally mediated perovskite crystallization in governing film orientation, paving the way for realizing crystal-oriented perovskite films toward efficient and durable facet-dependent PSCs.

■ ASSOCIATED CONTENT

Supporting Information

The Supporting Information is available free of charge at https://pubs.acs.org/doi/10.1021/acs.jpcc.6c01538.

Calculation methods used for testing results of perovskite films and the resultant devices, XRD patterns, perovskite photograph evolution, perovskite surface morphologies and potential distribution, photovoltaic parameter distribution, $J-V$ measurements, UV−vis absorption spectra, and XPS spectra (PDF)

■ AUTHOR INFORMATION

Corresponding Author

Meicheng Li − *State Key Laboratory of Alternate Electrical Power System with Renewable Energy Sources, School of New Energy, North China Electric Power University, Beijing 102206, China*; orcid.org/0000-0002-0731-741X; Email: mcli@ncepu.edu.cn

Authors

Hai-Fang Li − *State Key Laboratory of Alternate Electrical Power System with Renewable Energy Sources, School of New Energy, North China Electric Power University, Beijing 102206, China*

Zhiyu Zhang − *State Key Laboratory of Alternate Electrical Power System with Renewable Energy Sources, School of New Energy, North China Electric Power University, Beijing 102206, China*

Teng Xu − *State Key Laboratory of Alternate Electrical Power System with Renewable Energy Sources, School of New Energy, North China Electric Power University, Beijing 102206, China*

Shujie Qu − *State Key Laboratory of Alternate Electrical Power System with Renewable Energy Sources, School of New Energy, North China Electric Power University, Beijing 102206, China*

Chuanmin Yao − *State Key Laboratory of Alternate Electrical Power System with Renewable Energy Sources, School of New Energy, North China Electric Power University, Beijing 102206, China*

Tongtong Jiang − *State Key Laboratory of Alternate Electrical Power System with Renewable Energy Sources, School of New Energy, North China Electric Power University, Beijing 102206, China*

Zhiwei Wang − *State Key Laboratory of Alternate Electrical Power System with Renewable Energy Sources, School of New Energy, North China Electric Power University, Beijing 102206, China*

Jinhui Wang − *State Key Laboratory of Alternate Electrical Power System with Renewable Energy Sources, School of New Energy, North China Electric Power University, Beijing 102206, China*

Zeze Chen − *State Key Laboratory of Alternate Electrical Power System with Renewable Energy Sources, School of New Energy, North China Electric Power University, Beijing 102206, China*

Shuainan Li − *State Key Laboratory of Alternate Electrical Power System with Renewable Energy Sources, School of New Energy, North China Electric Power University, Beijing 102206, China*

Bingbing Fan − *State Key Laboratory of Alternate Electrical Power System with Renewable Energy Sources, School of New Energy, North China Electric Power University, Beijing 102206, China*

Peng Cui − *State Key Laboratory of Alternate Electrical Power System with Renewable Energy Sources, School of New Energy, North China Electric Power University, Beijing 102206, China*

Xing Zhao − *State Key Laboratory of Alternate Electrical Power System with Renewable Energy Sources, School of New Energy, North China Electric Power University, Beijing 102206, China*; orcid.org/0000-0002-3323-2014

Yingfeng Li − *State Key Laboratory of Alternate Electrical Power System with Renewable Energy Sources, School of New Energy, North China Electric Power University, Beijing 102206, China*

Complete contact information is available at: https://pubs.acs.org/10.1021/acs.jpcc.6c01538

Notes

The authors declare no competing financial interest.

■ ACKNOWLEDGMENTS

The authors greatly acknowledge the financial support from the Beijing Natural Science Foundation (Nos. 2222077 and Z240024), the National Natural Science Foundation of China (Nos. 52232008 and 22409061), the Fundamental Research Funds for the Central Universities (Nos. 2024JC005 and 2022MS028), and the "Double First-Class" Program of North China Electric Power University. The authors thank Dr. Hao Huang, Dr. Xin Sun, and Dr. Liang Li at the School of New Energy, North China Electric Power University, for their insightful discussions.

■ REFERENCES

(1) Han, J.; Park, K.; Tan, S.; Vaynzof, Y.; Xue, J.; Diau, E. W. G.; Bawendi, M. G.; Lee, J. W.; Jeon, I. Perovskite Solar Cells. *Nat. Rev. Methods Primers* **2025**, *5*, 3.

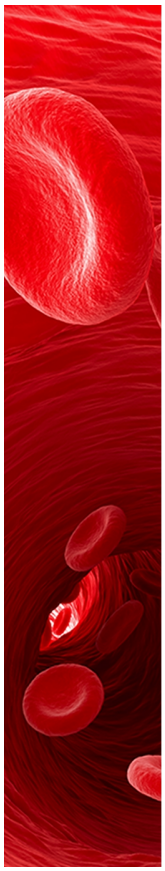
(2) Yang, R.; Yang, D.; Liu, S. F. High-Performance All-Inorganic Cesium Halide Perovskite Solar Cells. *Chem. Rev.* **2026**, *126*, 1408−1469.
(3) Li, B.; Shen, T.; Yun, S. Recent Progress of Crystal Orientation Engineering in Halide Perovskite Photovoltaics. *Mater. Horiz.* **2023**, *10*, 13−40.
(4) Ma, C.; Eickemeyer, F. T.; Lee, S.-H.; Kang, D.-H.; Kwon, S. J.; Grätzel, M.; Park, N.-G. Unveiling Facet-Dependent Degradation and Facet Engineering for Stable Perovskite Solar Cells. *Science* **2023**, *379*, 173−178.
(5) Zhumekenov, A. A.; Sharma, A.; Jamolov, A.; Nambiar, A.; Abuzeid, H. R.; Miftahullatif, E. B.; Singhal, N.; Pullarkat, S. A.; Hippalgaonkar, K.; Mathews, N. Expanding the Solvent Library for Halide Perovskites via Amine Additives. *ACS Materials Lett.* **2026**, *8*, 446−454.
(6) Xu, L.; Ji, H.; Qiu, W.; Wang, X.; Liu, Y.; Li, Y.; Li, J.; Zhang, X.; Zhang, D.; Wang, J.; Tao, Y.; Li, M.; Chen, R. Enhanced Resonance for Facilitated Modulation of Large-Area Perovskite Films with Stable Photovoltaics. *Adv. Mater.* **2023**, *35*, No. 2301752.
(7) Zhou, B.; Zhao, P.; Guo, J.; Hu, S.; Guo, X.; Liu, J.; Li, C. Solvent-Additive Cascade Engineering Enables Single-Oriented Perovskite Films with Facet-Driven Performance and Stability. *Energy Environ. Sci.* **2025**, *18*, 9865−9876.
(8) Tang, G.; You, P.; Tai, Q.; Yang, A.; Cao, J.; Zheng, F.; Zhou, Z.; Zhao, J.; Chan, P. K. L.; Yan, F. Solution-Phase Epitaxial Growth of Perovskite Films on 2D Material Flakes for High-Performance Solar Cells. *Adv. Mater.* **2019**, *31*, No. 1807689.
(9) Liu, X.; Wu, Z.; Zhong, H.; Wang, X.; Yang, J.; Zhang, Z.; Han, J.; Oron, D.; Lin, H. Epitaxial 2D PbS Nanosheet-Formamidinium Lead Triiodide Heterostructure Enabling High-Performance Perovskite Solar Cells. *Adv. Funct. Mater.* **2023**, *33*, No. 2304140.
(10) Zhao, W.; Wu, M.; Liu, Z.; Yang, S.; Li, Y.; Wang, J.; Yang, L.; Han, Y.; Liu, S. (. Orientation Engineering via 2D Seeding for Stable 24.83% Efficiency Perovskite Solar Cells. *Adv. Energy Mater.* **2023**, *13*, No. 2204260.
(11) Chen, J.; She, X.; Mi, S.; Li, Z.; Yin, X.; Li, Z.; He, C.; An, X. Template-Assisted Epitaxial Growth of (111)-Dominated $FAPbI_3$ for Enhanced Photovoltaic Performance and Stability. *Chem. Commun.* **2025**, *61*, 19285−19288.
(12) Zhang, Y.; Fu, X.; Su, Y.; Wu, Y. Orientated Crystallization of $MAPbI_3$ Using Template Method for Efficient and Stable Solar Cells. *Mater. Today Energy* **2025**, *49*, No. 101820.
(13) Ren, Y.; Fu, H.; Sun, Y.; Li, Z.; Guo, X.; An, X. Building (001) Oriented $FAPbI_3$ Films for High-Performing Perovskite Solar Cells. *Chem. Commun.* **2024**, *60*, 3673−3676.
(14) Shi, Z.; Liu, H.; Jiao, H.; Li, M.; Ni, Z.; Zhao, L.; Huang, J. Self-Regulated facet Stability During Solution Growth of Perovskite Crystals. *Nat. Synth.* **2025**, *4*, 1088−1094.
(15) Sun, X.; Li, D.; Zhao, L.; Zhang, Y.; Hu, Q.; Russell, T. P.; Liu, F.; Wei, J.; Li, H. (111)-Dominated Perovskite Films by Antisolvent Engineering. *Adv. Mater.* **2023**, *35*, No. 2301115.
(16) Wang, X.; Han, Z.; Gao, F.; Luo, C.; Zhao, Q. Facet Orientation and Intermediate Phase Regulation via a Green Antisolvent for High-Performance Perovskite Solar Cells. *Solar RRL* **2022**, *6*, No. 2100973.
(17) Li, D.; Sun, X.; Zhang, Y.; Guan, Z.; Yue, Y.; Wang, Q.; Zhao, L.; Liu, F.; Wei, J.; Li, H. Uniaxial-Oriented Perovskite Films with Controllable Orientation. *Adv. Sci.* **2024**, *11*, No. 2401184.
(18) Zhou, B.; Zhao, P.; Guo, J.; Hu, S.; Guo, X.; Liu, J.; Li, C. Unveiling the Importance of Nondominant Facets in (111)-Dominated Perovskite Films. *ACS Appl. Mater. Interfaces* **2025**, *17*, 22715−22726.
(19) Xu, Z.; Liu, Z.; Li, N.; Tang, G.; Zheng, G.; Zhu, C.; Chen, Y.; Wang, L.; Huang, Y.; Li, L.; Zhou, N.; Hong, J.; Chen, Q.; Zhou, H. A Thermodynamically Favored Crystal Orientation in Mixed Formamidinium/Methylammonium Perovskite for Efficient Solar Cells. *Adv. Mater.* **2019**, *31*, No. 1900390.
(20) Zheng, X.; Hou, Y.; Bao, C.; Yin, J.; Yuan, F.; Huang, Z.; Song, K.; Liu, J.; Troughton, J.; Gasparini, N.; Zhou, C.; Lin, Y.; Xue, D.-J.; Chen, B.; Johnston, A. K.; Wei, N.; Hedhili, M. N.; Wei, M.; Alsalloum, A. Y.; Maity, P.; Turedi, B.; Yang, C.; Baran, D.; Anthopoulos, T. D.; Han, Y.; Lu, Z.-H.; Mohammed, O. F.; Gao, F.; Sargent, E. H.; Bakr, O. M. Managing Grains and Interfaces via Ligand Anchoring Enables 22.3%-Efficiency Inverted Perovskite Solar Cells. *Nat. Energy* **2020**, *5*, 131−140.
(21) Jiang, X.; Liu, B.; Wu, X.; Zhang, S.; Zhang, D.; Wang, X.; Gao, S.; Huang, Z.; Wang, H.; Li, B.; Xiao, Z.; Chen, T.; Jen, A. K.; Xiao, S.; Yang, S.; Zhu, Z. Top-Down Induced Crystallization Orientation toward Highly Efficient p-i-n Perovskite Solar Cells. *Adv. Mater.* **2024**, *36*, No. 2313524.
(22) Liu, X.; Jiang, X.; Yin, Y.; Zhang, J.; Tian, H.; Guo, J.; Guo, X.; Li, C. Dominating (111) Facets with Ordered Stacking in Perovskite Films. *Energy Environ. Sci.* **2024**, *17*, 6058−6067.
(23) Ma, C.; Kang, M.-C.; Lee, S.-H.; Kwon, S. J.; Cha, H.-W.; Yang, C.-W.; Park, N.-G. Photovoltaically Top-Performing Perovskite Crystal Facets. *Joule* **2022**, *6*, 2626−2643.
(24) Zhang, S.; Zhou, Y.; Shen, Z.; Li, Y.; Song, J.; Gao, Y.; Wang, Z.; Zhang, B.; Chen, C.; Liu, R.; Liu, Y.; Cao, R.; Li, H.; Li, F. High-Efficiency and Stable Perovskite Solar Cells via Bidentate Chelation for Facet-Engineered Growth of $FAPbI_3$ (111) Crystals. *Chem. Eng. J.* **2025**, *516*, No. 164079.
(25) Li, Y.; Zhang, Z.; Zhang, H.; Liu, Y.; Gao, H.; Mao, Y. Preparation of (111) Facet-Dominated Perovskite Films for Highly Efficient and Stable Perovskite Solar Cells. *ACS Appl. Mater. Interfaces* **2025**, *17*, 48231−48239.
(26) Feng, W.; Liu, X.; Liu, G.; Yang, G.; Fang, Y.; Shen, J.; Jin, B.; Chen, X.; Huang, Y.; Wang, X.; Wu, C.; Yang, S.; Wu, W. Blade-Coating (100)-Oriented α-$FAPbI_3$ Perovskite Films via Crystal Surface Energy Regulation for Efficient and Stable Inverted Perovskite Photovoltaics. *Angew. Chem., Int. Ed.* **2024**, *63*, No. e202403196.
(27) Zhang, K.; Ding, B.; Wang, C.; Shi, P.; Zhang, X.; Liu, C.; Yang, Y.; Gao, X.; Wang, R.; Tao, L.; Brooks, K. G.; Dai, S.; Dyson, P. J.; Nazeeruddin, M. K.; Ding, Y. Highly Efficient and Stable $FAPbI_3$ Perovskite Solar Cells and Modules Based on Exposure of the (011) Facet. *Nano-Micro Lett.* **2023**, *15*, 138.
(28) Wang, K.; Xu, Z.; Li, K.; Li, R.; Guo, Z.; Yang, Y.; Huang, J.; Mohammed, O. F.; Zang, Z. Amidino-Based Ligand Enables Oriented Crystallization and Boosted Carrier Extraction for Inverted Perovskite Solar Cells and Modules. *Joule* **2025**, *9*, No. 102044.
(29) Yang, T.; Yang, Y.; Niu, T.; Zhao, E.; Wu, N.; Wang, S.; Chen, X.; Wang, S.; Wang, Y.; Wu, Y.; Zhang, Z.; Ma, C.; Gong, Y.; Liu, D.; Zhao, K. Facet Orientation-Dependent Strain Relaxation Stabilizes $FAPbI_3$ Perovskite Solar Cells. *ACS Energy Lett.* **2025**, *10*, 427−438.
(30) Ma, C.; Kang, M.-C.; Lee, S.-H.; Zhang, Y.; Kang, D.-H.; Yang, W.; Zhao, P.; Kim, S.-W.; Kwon, S. J.; Yang, C.-W.; Yang, Y.; Park, N.-G. Facet-Dependent Passivation for Efficient Perovskite Solar Cells. *J. Am. Chem. Soc.* **2023**, *145*, 24349−24357.
(31) Zhou, J.; Chen, Y.; Shen, Y.; Peng, Y.; Wu, X.; Xie, Z.; Luo, C.; Deng, M.; Duan, Y.; Wu, Y.; Peng, Q. Tailoring Low-Miller-Index Crystal Facets Realizes Perovskite Solar Cells with Flat Grain-Boundary Grooves. *Angew. Chem., Int. Ed.* **2025**, *64*, No. e202511042.
(32) Chi, W.; Banerjee, S. K. Achieving Resistance against Moisture and Oxygen for Perovskite Solar Cells with High Efficiency and Stability. *Chem. Mater.* **2021**, *33*, 4269−4303.
(33) Kore, B. P.; Jamshidi, M.; Gardner, J. M. The Impact of Moisture on the Stability and Degradation of Perovskites in Solar Cells. *Mater. Adv.* **2024**, *5*, 2200−2217.
(34) Meng, H.; Mao, K.; Cai, F.; Zhang, K.; Yuan, S.; Li, T.; Cao, F.; Su, Z.; Zhu, Z.; Feng, X.; Peng, W.; Xu, J.; Gao, Y.; Chen, W.; Xiao, C.; Wu, X.; McGehee, M. D.; Xu, J. Inhibition of Halide Oxidation and Deprotonation of Organic Cations with Dimethylammonium Formate for Air-Processed p−i−n Perovskite Solar Cells. *Nat. Energy* **2024**, *9*, 536−547.
(35) Wang, S.; Gong, X.-Y.; Li, M.-X.; Li, M.-H.; Hu, J.-S. Polymers for Perovskite Solar Cells. *JACS Au* **2024**, *4*, 3400−3412.
(36) Yang, S.; Wang, Y.; Liu, P.; Cheng, Y. B.; Zhao, H. J.; Yang, H. G. Functionalization of Perovskite Thin Films with Moisture-Tolerant Molecules. *Nat. Energy* **2016**, *1*, 15016.

https://doi.org/10.1021/acs.jpcc.6c01538
J. Phys. Chem. C 2026, 130, 6973−6985

(37) Zhu, H.; Liu, Y.; Eickemeyer, F. T.; Pan, L.; Ren, D.; Ruiz-Preciado, M. A.; Carlsen, B.; Yang, B.; Dong, X.; Wang, Z.; Liu, H.; Wang, S.; Zakeeruddin, S. M.; Hagfeldt, A.; Dar, M. I.; Li, X.; Grätzel, M. Tailored Amphiphilic Molecular Mitigators for Stable Perovskite Solar Cells with 23.5% Efficiency. *Adv. Mater.* **2020**, *32*, No. 1907757.
(38) Yan, L.; Huang, H.; Cui, P.; Du, S.; Lan, Z.; Yang, Y.; Qu, S.; Wang, X.; Zhang, Q.; Liu, B.; Yue, X.; Zhao, X.; Li, Y.; Li, H.; Ji, J.; Li, M. Fabrication of Perovskite Solar Cells in Ambient Air by Blocking Perovskite Hydration with Guanabenz Acetate Salt. *Nat. Energy* **2023**, *8*, 1158−1167.
(39) Yan, L.; Huang, H.; Cui, P.; Yang, Y.; Su, Z.; Lu, Y.; Wang, M.; Lan, Z.; Qu, S.; Liu, B.; Sun, C.; Li, L.; Du, S.; Yang, F.; Gao, X.; Li, M. Moisture-Stable Intermediate Phase Manipulation for Efficient Perovskite Solar Cells Fabricated in Ambient Air. *ACS Energy Lett.* **2025**, *10*, 5156−5164.
(40) Gong, X.; Li, M.; Shi, X.-B.; Ma, H.; Wang, Z.-K.; Liao, L.-S. Controllable Perovskite Crystallization by Water Additive for High-Performance Solar Cells. *Adv. Funct. Mater.* **2015**, *25*, 6671−6678.
(41) Cao, J.; Zhang, X.; Miao, Y.; Li, W.; Zeng, X.; Yang, S.; Yan, C.; Lu, J.; Yang, W. Interactions Between H_2O and Lead Halide Perovskites: Recent Progress and Applications. *Matter* **2024**, *7*, 3728−3755.
(42) Wang, C.; He, B.; Hui, W.; Su, Z.; Chen, L.; Du, W.; Zhang, L.; Zhang, J.; Fu, M.; Wang, H.; Sun, B.; Wen, W.; Wang, S.; Lou, L.; Hou, C.; Zheng, G.; Song, L.; Chen, Y.; Gao, X. Controlling Water for Enhanced Homogeneities in Perovskite Solar Cells with Remarkable Reproducibility. *Adv. Funct. Mater.* **2024**, *34*, No. 2403690.
(43) Xie, Y.; Chen, S.; Gu, Z.; Xu, K.; Chao, L.; Xia, Y. Role of Water in the Stability and Efficiency of Ionic Liquid-Based Perovskite Solar Cells. *J. Phys. Chem. Lett.* **2025**, *16*, 1597−1603.
(44) Qu, S.; Huang, H.; Wang, J.; Cui, P.; Li, Y.; Wang, M.; Li, L.; Yang, F.; Sun, C.; Zhang, Q.; Zhu, P.; Wang, Y.; Li, M. Revealing and Inhibiting the Facet-Related Ion Migration for Efficient and Stable Perovskite Solar Cells. *Angew. Chem., Int. Ed.* **2024**, *64*, No. e202415949.
(45) Lin, Z. Q.; Qiao, H. W.; Zhou, Z. R.; Hou, Y.; Li, X.; Yang, H. G.; Yang, S. Water Assisted Formation of Highly Oriented $CsPbI_2Br$ Perovskite Films with the Solar Cell Efficiency Exceeding 16%. *J. Mater. Chem. A* **2020**, *8*, 17670−17674.
(46) Liu, K.; Luo, Y.; Jin, Y.; Liu, T.; Liang, Y.; Yang, L.; Song, P.; Liu, Z.; Tian, C.; Xie, L.; Wei, Z. Moisture-Triggered Fast Crystallization Enables Efficient and Stable Perovskite Solar Cells. *Nat. Commun.* **2022**, *13*, 4891.
(47) Fan, W.; Deng, K.; Shen, Y.; Bai, Y.; Li, L. Moisture-Accelerated Precursor Crystallisation in Ambient Air for High-Performance Perovskite Solar Cells toward Mass Production. *Angew. Chem., Int. Ed.* **2022**, *61*, No. e202211259.
(48) Ma, Y.; Luo, C.; Zhan, C.; Wang, K.; He, J.; Gao, P.; Bi, Z.; Ma, Y.; Zhao, Q. Crystallization-Activated Moisture Barrier for High-Tolerance Manufacturing of Perovskite Solar Cells. *Sci. Adv.* **2025**, *11*, No. eady5703.
(49) Xu, L.; Qian, W.; Zhou, Y.; Wei, Z.; Wang, H.; Lv, W.; Li, J.; Huang, W.; Yao, L.; Chen, R.; Huang, W. In Situ Cation Exchange Enables Air-Processed Inverted Perovskite Solar Cells with over 25% Efficiency and Enhanced Stability. *Angew. Chem., Int. Ed.* **2025**, *64*, No. e202503702.
(50) Hidalgo, J.; Perini, C. A. R.; Castro-Mendez, A.-F.; Jones, D.; Köbler, H.; Lai, B.; Li, R.; Sun, S.; Abate, A.; Correa-Baena, J.-P. Moisture-Induced Crystallographic Reorientations and Effects on Charge Carrier Extraction in Metal Halide Perovskite Solar Cells. *ACS Energy Lett.* **2020**, *5*, 3526−3534.
(51) Xi, J.; Yuan, J.; Yan, X.; Binks, D.; Tian, J. Gradient Annealing of Halide Perovskite Films for Improved Performance of Solar Cells. *ACS Appl. Energy Mater.* **2020**, *3*, 8130−8134.
(52) Wang, Z.; Chen, P.; Luo, J.; Ouyang, Z.; Sun, M.; Hu, Q.; Xie, W.; Liu, P.; Chen, K. Gradient Thermal Annealing Assisted Perovskite Film Crystallization Regulation for Efficient and Stable Photovoltaic-Photodetection Bifunctional Device. *Small Methods* **2025**, *9*, No. 2401098.
(53) Zou, S.; Zhang, J.; Xin, Y.; Jin, J.; Liu, G.; Yan, X.; Huang, J. Moisture-Inhibited Deprotonation at the Buried Interface Enables Efficient Perovskite Solar Cells with a High Fill Factor of Over 86%. *Energy Environ. Sci.* **2025**, *18*, 3385−3394.
(54) Zhang, Q.; Huang, H.; Yang, Y.; Wang, M.; Qu, S.; Lan, Z.; Jiang, T.; Wang, Z.; Du, S.; Lu, Y.; Suo, Y.; Cui, P.; Li, M. A Universal Ternary Solvent System of Surface Passivator Enables Perovskite Solar Cells with Efficiency Exceeding 26%. *Adv. Mater.* **2024**, *36*, No. 2410390.
(55) Fang, Z.; Yan, N.; Liu, S. Modulating Preferred Crystal Orientation for Efficient and Stable Perovskite Solar Cells-From Progress to Perspectives. *InfoMat* **2022**, *4*, No. e12369.
(56) Chen, Y.; Wang, K.; Han, Y.; Chen, W.; Yang, Y.; Qi, H.; Yang, F.; Tong, Y.; Wang, H. Tailored Crystallization and Defect Control via Acetamide Derivatives for Efficient Tin Perovskite Solar Cells. *ACS Nano* **2025**, *19*, 32270−32279.
(57) Li, C.; Park, H.; Qiu, S.; Streller, F.; Zhang, K.; Peng, Z.; Byun, J.; Tian, J.; Maiti, S.; Xie, Z.; Dong, L.; Liu, C.; Le Corre, V. M.; Shang, Y.; Wu, J.; Zhang, J.; Feng, M.; Späth, A.; Forberich, K.; Osvet, A.; Heumueller, T.; Christiansen, S. H.; Halik, M.; Fink, R. H.; Unruh, T.; Li, N.; Lüer, L.; Brabec, C. J. Controlling Intermediate Phase Formation to Enhance Photovoltaic Performance of Inverted FA-based Perovskite Solar Cells. *ACS Energy Lett.* **2024**, *9*, 5434−5443.
(58) Wang, Y.; Zhang, Z.; Zeng, Z.; Zhang, Y.; Hu, T.; Bi, L.; Yang, Y.; Ouyang, S.; Hao, X.; Xu, C.; Cheng, Y.; Hu, H.; Jen, A. K. Y.; Ho, J. C.; Wu, T.; Tsang, S. W. Intermediate State Formation Extends the Ambient Temperature Processing Window of Solution-Processed Perovskite Solar Cells. *ACS Energy Lett.* **2025**, *10*, 647−657.
(59) Tang, S.; Zhang, Z.; Yu, Y.; Liu, X.; He, D.; Shai, X.; Zhang, J.; Feng, J.; Yi, J.; Chen, C.; Yu, H.; Chen, J. Crystallization Modulation and Comprehensive Defect Passivation by Carbonyl Functionalized Spacer Cation Towards High-Performance Inverted Perovskite Solar Cells. *Angew. Chem., Int. Ed.* **2025**, *64*, No. e202425605.
(60) Yan, S.; Zhang, B.; Zhang, W.; Chen, K.; He, Z.; Sun, Y.; Yin, H.; Ouyang, Z.; Li, X.; Xiao, B. Interface Molecular Orientation Engineering-Induced Field Reversal for Efficient Inverted Perovskite Solar Cells. *Energy Environ. Sci.* **2025**, *18*, 10494−10503.
(61) Jiang, Q.; Zhao, Y.; Zhang, X.; Yang, X.; Chen, Y.; Chu, Z.; Ye, Q.; Li, X.; Yin, Z.; You, J. Surface Passivation of Perovskite Film for Efficient Solar Cells. *Nat. Photonics* **2019**, *13*, 460−466.
(62) Shi, Z.; Liu, S.; Luo, R.; Ma, J.; Tian, H.; Wang, X.; Dong, Z.; Guo, X.; Chen, J.; Feng, J.; Xiao, C.; Wu, Y.; Hu, W.; Hou, Y. Ligand-Mediated Surface Reaction for Achieving Pure 2D Phase Passivation in High-Efficiency Perovskite Solar Cells. *J. Am. Chem. Soc.* **2025**, *147*, 1055−1062.
(63) Li, H.; Zhu, P.; Zhang, Z.; Sun, X.; Chen, S.; Xu, T.; Fan, B.; Cui, P.; Li, L.; Chu, L.; Li, M. Additive-Free Crystallization Modulation for Efficient Perovskite Solar Cells by a Transverse Pulsed Electric Field. *Small Methods* **2025**, *9*, No. e01431.
(64) Qu, S.; Sun, C.; Yang, F.; Huang, H.; Du, S.; Jiang, T.; Zhang, Q.; Yan, L.; Lan, Z.; Yang, Y.; Wang, Z.; Cui, P.; Li, M. Contextualized Synthesis of Phenanthroline-Based Isomeric Linkers at Heterointerfaces Enables Stable Inverted Perovskite Solar Cells. *Matter* **2026**, *9*, No. 102525.
(65) Zhao, Y.; Zhao, W.-H.; Ye, Y.-C.; Du, H.-W.; Ye, Q.-F.; Zhang, C.; Xie, H.; Dou, W.-D. Bidentate Phosphate Molecular Bridge Heals Buried Interface Defects for Stable NiO_x-Based Perovskite Solar Cells. *ACS Photonics* **2025**, *12*, 6884−6893.
(66) Xu, S.; Hu, Y.; Zhang, Y.; Xu, J.; Huang, Q.; Li, J.; Wang, M. Synergistic Surface Reconstruction and Defect Passivation via Guanidine Sulfonate for High-Efficiency Perovskite Photovoltaics. *J. Phys. Chem. Lett.* **2025**, *16*, 5221−5227.
(67) Liu, M.; Zhang, J.; Qin, S.; Miao, X.; Yuan, M.; Liu, Z.; Wang, Y.; Feng, Y.; Jiang, X.; Wu, R.; Yi, Y.; Meng, L.; Li, Y. Efficient and Stable p−i−n Perovskite Solar Cells Enabled by In Situ Functional Group Conversion. *J. Am. Chem. Soc.* **2024**, *146*, 32105−32116.
(68) Lan, Z.; Yang, Y.; Huang, H.; Du, S.; Zhang, Q.; Wang, Z.; Jiang, T.; Sun, C.; Qu, S.; Li, L.; Yan, L.; Cui, P.; Li, M. Interfacial Electrostatic Repulsion Inhibits Iodide Ion Migration for Enhancing

https://doi.org/10.1021/acs.jpcc.6c01538
J. Phys. Chem. C 2026, 130, 6973−6985

Reverse-Bias Stability of Perovskite Solar Cells. *Nat. Commun.* **2025**, *16*, 11407.
(69) Stoerzinger, K. A.; Hong, W. T.; Azimi, G.; Giordano, L.; Lee, Y.-L.; Crumlin, E. J.; Biegalski, M. D.; Bluhm, H.; Varanasi, K. K.; Shao-Horn, Y. Reactivity of Perovskites with Water: Role of Hydroxylation in Wetting and Implications for Oxygen Electrocatalysis. *J. Phys. Chem. C* **2015**, *119*, 18504−18512.


CAS BIOFINDER DISCOVERY PLATFORM™
CAS BIOFINDER HELPS YOU FIND YOUR NEXT BREAKTHROUGH FASTER
Navigate pathways, targets, and diseases with precision
Explore CAS BioFinder
CAS
A division of the American Chemical Society

https://doi.org/10.1021/acs.jpcc.6c01538
J. Phys. Chem. C 2026, 130, 6973−6985